

Nonlinear mechanisms in Al and Ti superconducting travelling-wave parametric amplifiers

Songyuan Zhao,^{1,*} S. Withington,¹ and C. N. Thomas¹

¹*Cavendish Laboratory, JJ Thomson Avenue, Cambridge CB3 OHE, United Kingdom.*

(Dated: February 23, 2022)

The underlying nonlinear mechanisms behind the operation of travelling-wave parametric amplifiers (TWPs) are important in determining their performance in terms of added noise, maximum gain, and bandwidth. We describe a method of characterising the underlying nonlinearity of a superconducting material in terms of its dissipative-reactive ratio and the response time of the underlying microscopic processes. We describe and calculate the different behaviour arising from the *equilibrium supercurrent nonlinearity*, which has low dissipation and fast response time, and the *non-equilibrium heating nonlinearity*, which has high dissipation and slow response time. We have fabricated TWPs based on Al and Ti, and characterised their nonlinearities using our analysis. For both Al and Ti, the measured dissipative-reactive ratios and response times are quantitatively similar to predictions for the non-equilibrium heating nonlinearity. In line with this, we were able to obtain more than 20 dB of peak power gain, although only over a narrow bandwidth of a few kilohertz.

Keywords: Superconducting parametric amplifiers, nonlinearity, non-equilibrium heating, supercurrent

I. INTRODUCTION

Superconducting travelling-wave parametric amplifiers (TWPs) are low-noise cryogenic amplifiers based on thin-film superconducting transmission lines [1]. These devices have received considerable interest in the last decade due to their potential to achieve high gain, broad-band amplification whilst having noise performance close to the quantum limit [2]. Currently, there are two main types of superconducting TWPs: Josephson travelling-wave parametric amplifiers (J-TWPs) and kinetic inductance travelling-wave parametric amplifiers (KI-TWPs). J-TWPs rely on the nonlinear inductance of tunnel junctions to achieve amplification. These devices benefit from the wealth of literature on designing resonant Josephson parametric amplifiers (JPAs) and Josephson junctions. However, the saturation power of J-TWPs are limited by the same junction critical current as their JPAs counterpart, and they may, as a result, be unsuitable for certain applications of broad-band parametric amplifiers. KI-TWPs, on the other hand, have high saturation power that are determined by the critical current of the material. They are suitable for applications such as the readout of large detector or qubit arrays. In this study, we focus on the underlying nonlinearities behind the operation of KI-TWPs.

KI-TWPs achieve amplification through wave-mixing processes induced by the nonlinear superconducting kinetic inductance. In general, the kinetic inductance per unit length L_k of a superconducting transmission line can be expanded as an infinite series of even powers of local line current I as follows:

$$L_k = L_{k,0} \left(1 + \frac{I^2}{I_*^2} + \frac{I^4}{I_{*,4}^4} + \dots \right), \quad (1)$$

where I_* and $I_{*,4}$ are the scales of the quadratic and quartic orders of nonlinearity respectively [1, 3–5], and $L_{k,0}$

is the kinetic inductance per unit length in the absence of inductive nonlinearity. The odd powers of dependence on current must vanish since, for a infinitesimal segment of superconducting transmission line, the kinetic inductance has the same value whether a $+I$ current is applied or a $-I$ current is applied. This symmetry can be broken through the application of a DC bias current, i.e. $I \rightarrow I_{DC} + I_{RF}$, where I_{DC} is the DC current and I_{RF} is the RF current. In the presence of a DC-bias, the kinetic inductance also depends on the odd powers of the RF current. As a result of this reactive kinetic inductance nonlinearity, when a strong pump current propagates with a weak signal current along a TWP, energy is transferred from the pump to the signal, thereby achieving parametric amplification [1, 6]. The form of inductance given in equation (1) can arise through different underlying physical contributions, such as the *equilibrium supercurrent nonlinearity* and the *non-equilibrium heating nonlinearity*. The meaning behind these terms will be discussed in the theory section of this work.

It is important to understand the nonlinear mechanisms behind the amplification process for any particular combination of material and geometry. In particular, the dissipative aspect and the response time of a mechanism can have profound impact on the amplification performance of a device. Firstly, the reactive nonlinearity may be accompanied by a strong dissipative nonlinearity. This dissipative nonlinearity will attenuate the maximum achievable power gain. Secondly, the power dissipated by the dissipative nonlinearity can raise the temperature of the device and degrade its performance. Thirdly, a dissipative nonlinearity is likely to alter the noise behaviour of the device, e.g. altering the thermal noise output by changing the level of dissipation, or by resulting in additional modulation of the noise. Understanding the magnitude of the dissipative nonlinearity is therefore important in determining if a particular TWP can, in theory, achieve amplification and approach the quantum

limit [7]. Lastly, as we shall show in this study, the response time of a nonlinear mechanism imposes a strong restriction on the bandwidth of a TWPA. In the case of non-equilibrium heating nonlinearity, the bandwidth is restricted to the range of a few kHz to a few MHz, depending on the material. This severely undermines the advantage of the broad-band travelling-wave geometry. A proper understanding of the underlying nonlinear mechanisms will inform the choice of material and the design of a TWPA so as to avoid these limitations.

In this study, we present theory and measurements to investigate the nonlinear mechanisms of Al and Ti TW-PAs. We characterise the nonlinear mechanisms in terms of dissipative-reactive ratios and response times. Measurements of both parameters can be performed using the same transmission line structure as the travelling-wave amplifier itself, as opposed to requiring a separate fabrication of other geometries such as resonators. We calculate the expected values of dissipative-reactive ratios for both the equilibrium supercurrent nonlinearity as well as the non-equilibrium heating nonlinearity. We also present a response time model of the nonlinear inductance, and show that the model predicts characteristic features in the measured gain profiles, such as bandwidth limitations and post-gain dip structures. The effects of reactive, dissipative, and rate-limited nonlinearity are also discussed extensively, in the context of resonator parametric amplifiers, in an upcoming paper [8]. In the experimental section, we present our measurements of Al and Ti TW-PAs that we have fabricated. Our measurements show significant dissipative nonlinearities in line with the order of magnitude predicted by the non-equilibrium heating nonlinearity. Further, our measurements of gain profiles confirm the characteristic features of our response time model of nonlinear inductance. Together, these measurements demonstrate that the nonlinear responses of Al and Ti likely contain significant contributions from non-equilibrium heating nonlinearity. In line with this we were able to obtain more than 20 dB of peak power gain, although only over a narrow bandwidth of a few kilohertz.

II. NONLINEAR MECHANISMS

A. Overview of mechanisms

In this work, we focus on two important effects of currents that have been widely observed in superconducting films [3, 9–13]: 1) modification of the quasiparticle density of states and therefore the equilibrium charge carrier distribution, and 2) non-equilibrium power absorption and sub-gap pair-breaking. We shall refer to the first effect as *equilibrium supercurrent nonlinearity*, and the second effect as *non-equilibrium heating nonlinearity*.

In both the BCS theory of superconductivity as well as the Ginzburg-Landau (GL) theory, the presence of a supercurrent requires the Cooper pairs to have a non-

zero superfluid velocity. The equilibrium supercurrent nonlinearity arises as a result of modifications to the superconducting properties in the presence of this superfluid velocity. This nonlinearity can be thought of as an equilibrium effect since the superconducting properties are equilibrium solutions of the BCS/GL theories in the presence of a superfluid velocity term. The supercurrent nonlinearity manifests itself in a variety of measurable properties, such as modified quasiparticle density of states [14], suppressed pair-breaking frequency threshold [15], and suppressed transition temperature [5]. Importantly to the operation of TW-PAs, the kinetic inductance has a dependence on the supercurrent through this effect [5]. This supercurrent-dependence is often referred to as the nonlinear kinetic inductance or the supercurrent nonlinearity, depending on the emphasis. For the equilibrium supercurrent nonlinearity, in the limit of thin and narrow films, the scaling terms in the kinetic inductance nonlinearity, I_* and $I_{*,4}$ in equation (1), relate to the critical current I_c by [6]

$$I_* = \frac{3\sqrt{3}}{2} I_c \quad (2)$$

$$I_{*,4} = \frac{1}{\sqrt[4]{3}} I_* . \quad (3)$$

Non-equilibrium heating nonlinearity is another nonlinear effect that emerges in the presence of a strong RF supercurrent. Measurements of superconducting resonators have shown that microwave readout power at sub-gap frequencies results in an increased quasiparticle population that contributes to noise and shortens quasiparticle lifetime [11, 12, 16, 17]. Microscopically, this observation has been explained by absorption of multiple sub-gap *photons* leading to quasiparticles emitting above-gap *phonons*. The above-gap phonons in turn break Cooper pairs and result in an increased quasiparticle population [11]. This pair-breaking interaction results in non-equilibrium distribution of quasiparticles and Cooper pairs. The non-equilibrium heating nonlinearity manifests itself strongly in both dissipative and reactive properties of a superconducting transmission line. The kinetic inductance arises through the kinetic energy of the Cooper pairs. In the Drude model, the kinetic inductance is inversely proportional to the pair population [6]. By suppressing the Cooper pair population and increasing the quasiparticle population, non-equilibrium heating likewise results in current-dependence in the kinetic inductances.

While these two types of nonlinear phenomena have different origins, a superconductor that conducts a strong RF current will unavoidably display both effects to different magnitudes. It can be difficult to distinguish the two phenomena if one looks at the reactive nonlinearity only: in both theories, the kinetic inductance has the same functional form $L_k = L_{k,0}[1 + (I/I_*)^2]$, keeping the lowest order term on current. The sign of the quadratic term is the same for both effects since both nonlinearities suppress the population of Cooper pairs and, as a

result, increase the kinetic inductance. The two types of nonlinearity can, however, be distinguished by considering their effects on the ratio between the dissipative and reactive nonlinearities and the frequency profile of the wave-mixing processes. These important differences will be discussed in detail in the main body of this paper.

The relative importance of the two phenomena at a particular readout power level is determined by their onset powers, which is the power required for each nonlinearity to result in the same change in the magnitude of the complex conductivities. For the equilibrium supercurrent nonlinearity, in the limit where the kinetic inductance ratio is close to unity, the onset power can be related straightforwardly from I_* through the characteristic impedance Z_0 . For the non-equilibrium heating nonlinearity, the onset power can be calculated using the Rothwarf-Taylor equations or more detailed non-equilibrium modelling [18, 19]. When a device is operated in a power regime that is between the onset powers of the two types of nonlinear phenomena, its behaviour will appear to be dominated by the nonlinear mechanism that has the lower onset power. When the operating power is stronger than the onset powers of both mechanisms, the behaviour of a device will be complicated by the interaction between the two mechanisms. This interaction is beyond the scope of this study.

Whilst we have focused on understanding the nonlinearity of a superconductor conceptually in terms of two well-established models, there are other interesting models of nonlinear superconductivity published in recent decades [20–23]. There are also other sources of nonlinear behaviour that are driven by current on a superconductor, such as superconducting weak links and local populations of two-level-systems. A detailed discussion of these effects will not be the focus this study. Weak link nonlinearity is present when there are superconducting weak link structures in the superconducting films [24]. As yet, these structures have not been reported in the literature to appear in KI-TWPAs. Two-level-system effects, on the other hand, are strongly suppressed at high power levels [25]. Since TWPAs operate at high power levels in order to achieve efficient nonlinear wave-mixing, it is sufficient to exclude two-level-system nonlinearity at the present level of analysis.

B. Dissipative-reactive ratios

A general observation in nature is that dissipative and reactive effects are often related, for example through causality [26, 27]. In this section, we characterise the ratio between the two effects that arise from equilibrium supercurrent nonlinearity and non-equilibrium heating. We have chosen to compare their effect on the complex conductivities $\sigma = \sigma_1 - i\sigma_2$, where σ_1 is the dissipative conductivity and σ_2 is the reactive conductivity. The effect of the current on σ can be straightforwardly inferred from experimental measurements of signal attenuation

and phase shift, as shall be shown in the measurements section. In the presence of a strong supercurrent, σ is modified to be $\sigma + \delta\sigma$, where $\delta\sigma$ characterises the effect that the nonlinear mechanisms have on the complex conductivities, and is given by $\delta\sigma = \delta\sigma_1 - i\delta\sigma_2$. We define the dissipative-reactive ratio κ to be $\kappa = |\delta\sigma_1/\delta\sigma_2|$.

The effect of the equilibrium nonlinearity on the dissipative-reactive ratio can be calculated using the analysis routine described in [5, 6]. The analysis routine is based on the Usadel equations [28] which is reformulated from the BCS theory of superconductivity and is suitable for dirty limit materials or thin-film superconductors [29]. When the transverse dimensions of the superconducting transmission line are small compared to the superconducting coherence length ξ_0 , and when then supercurrent is conducted along the length of the transmission line, the Usadel equations have the following form [14]:

$$E \sin \theta + i\Gamma \cos \theta \sin \theta - i\Delta \cos \theta = 0, \quad (4)$$

$$N_0 V \int_0^{\hbar\omega_D} dE \tanh\left(\frac{E}{2k_B T}\right) \text{Im}(\sin \theta) = \Delta, \quad (5)$$

where θ is a complex variable dependent on energy E which parameterises the superconducting properties, N_0 is the single spin density of states at the Fermi surface, V is the interaction potential, Δ is the superconducting order parameter, $\hbar\omega_D$ is the Debye energy, T is the temperature of the superconducting film, D is the diffusivity constant, given by $D = \sigma_N/(N_0 e^2)$ [30], e is the elementary charge, $\text{Im}(x)$ takes the imaginary part of x , and finally σ_N is the normal state conductivity, at T just above the superconducting transition temperature T_c . The effect of the current is encapsulated using the depairing term Γ .

Although not needed for this study, solutions of superconducting properties in term of Γ can be expressed in terms of supercurrent density \vec{j} by:

$$\Gamma = \frac{\hbar}{2D_S} \vec{v}_s^2 \quad (6)$$

$$\vec{j} = q_{\text{cp}} N_{\text{N, cp}} \vec{v}_s, \quad (7)$$

$$N_{\text{N, cp}} = \frac{1}{2} N_0 \int_0^{\infty} \tanh\left(\frac{E}{2k_B T}\right) \text{Im}(\sin^2 \theta), \quad (8)$$

where $q_{\text{cp}} = 2e$ is the charge of a Cooper pair, \vec{v}_s is the superfluid velocity, and $N_{\text{N, cp}}$ is the number density of Cooper pairs. At absolute zero temperature, the critical current density is reached when $\Gamma = \Delta_0/4$, where Δ_0 is the density of states gap at absolute zero, given in the BCS theory by $\Delta_0 = 1.764 k_B T_c$, where k_B is the Boltzmann constant. Thus the range of physically meaningful Γ/Δ_0 lies between 0 and 0.25 for this study.

Numerically, the Usadel equations are used to calculate the effect of Γ on the densities of states $\cos \theta$ and $\sin \theta$. Afterwards, the densities of states are integrated using Nam's equations [31, 32] to obtain the complex conductivities.

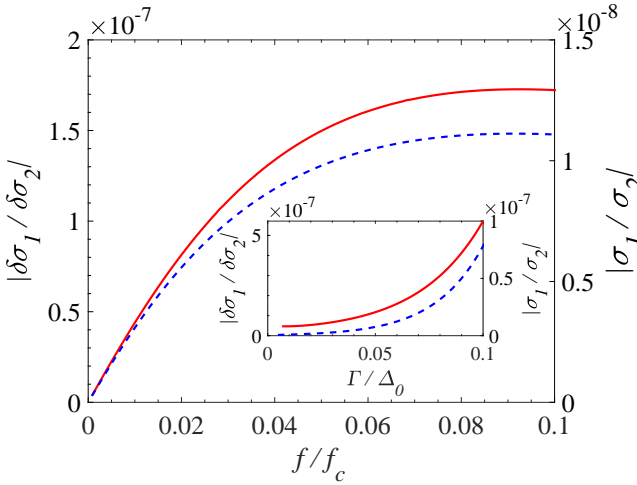


FIG. 1. Main figure: solid red line, left axis: dissipative-reactive ratio $\kappa = \delta\sigma_1/\delta\sigma_2$ arising from the equilibrium nonlinearity plotted against scaled frequency f/f_c ; dashed blue line, right axis: ratio of conductivities σ_1/σ_2 arising from the equilibrium nonlinearity plotted against frequency f/f_c . Calculation is performed for Al at temperature $T = 0.1$ K and depairing term $\Gamma/\Delta_0 = 0.05$.

Inset: solid red line, left axis: dissipative-reactive ratio $\kappa = \delta\sigma_1/\delta\sigma_2$ arising from the equilibrium nonlinearity plotted against scaled depairing term Γ/Δ_0 ; dashed blue line, right axis: ratio of conductivities σ_1/σ_2 arising from the equilibrium nonlinearity plotted against scaled depairing term Γ/Δ_0 . Calculation is performed for Al at temperature $T = 0.1$ K and frequency $f = 3$ GHz.

The dissipative-reactive ratio κ arising from the equilibrium nonlinearity is shown in figure 1 for Al at temperature $T = 0.1$ K. The main figure shows the dependence of κ on scaled frequency f/f_c whereas the inset shows the dependence of κ on scaled depairing term Γ/Δ_0 . The scaling frequency f_c is the pair-breaking frequency of Al when $T \ll T_c$, given by $f_c = 2\Delta_0/h$, h is the Planck constant. The dissipative aspect of the equilibrium supercurrent nonlinearity remains very small compared to the reactive aspect when the supercurrent frequency is small compared to the pair-breaking frequency of the material, which is ~ 88 GHz for Al. On a travelling-wave transmission line, this small dissipative change can be extremely hard to measure because it is often overshadowed by other dissipation mechanisms such as dielectric loss. It can instead be observed experimentally by measuring the change in quality factor of a high-Q superconducting resonator in response to a biasing current [33].

The effect of non-equilibrium heating can be calculated by considering the change in σ_1 and σ_2 in response to a change in quasiparticle number density due to pair-breaking effects. This topic has been well studied in the context of kinetic inductance detectors and the results

are as follows [3]:

$$\frac{\delta\sigma_{1,2}}{\sigma_N} = \frac{\pi}{2N_0\hbar\omega} S_{1,2}(\omega, T, \Delta_0) \delta n_{qp} \quad (9)$$

$$S_1(\omega, T, \Delta_0) = \frac{2}{\pi} \sqrt{\frac{2\Delta_0}{\pi k_B T}} \sinh\left(\frac{\hbar\omega}{2k_B T}\right) K_0\left(\frac{\hbar\omega}{2k_B T}\right) \quad (10)$$

$$S_2(\omega, T, \Delta_0) = 1 + \sqrt{\frac{2\Delta_0}{\pi k_B T}} \exp\left(\frac{-\hbar\omega}{2k_B T}\right) I_0\left(\frac{\hbar\omega}{2k_B T}\right), \quad (11)$$

where I_0 and K_0 are the modified Bessel functions of the first and second kind respectively, \hbar is the reduced Planck constant, ω is the angular frequency, and δn_{qp} is the change in quasiparticle number density. Equation (9) gives the dissipative-reactive ratio to be $\kappa = |S_1/S_2|$. For BCS superconductors, both Δ_0 and f_c scale linearly with T_c according to $\Delta_0 = 1.764 k_B T_c$ and $f_c = 2\Delta_0/h$. As a result, equations (10) and (11) can be expressed generally in terms of scaled frequency f/f_c and scaled temperature T/T_c as follows:

$$S_1\left(\frac{f}{f_c}, \frac{T}{T_c}\right) = \frac{2}{\pi} \sqrt{\frac{2\alpha T_c}{\pi T}} \sinh\left(\alpha \frac{f}{f_c} \frac{T_c}{T}\right) K_0\left(\alpha \frac{f}{f_c} \frac{T_c}{T}\right) \quad (12)$$

$$S_2\left(\frac{f}{f_c}, \frac{T}{T_c}\right) = 1 + \sqrt{\frac{2\alpha T_c}{\pi T}} \exp\left(-\alpha \frac{f}{f_c} \frac{T_c}{T}\right) I_0\left(\alpha \frac{f}{f_c} \frac{T_c}{T}\right), \quad (13)$$

where $\alpha = 1.764$.

Figure 2 shows the dissipative-reactive ratio κ for BCS superconductors arising from non-equilibrium heating nonlinearity plotted against scaled frequency f/f_c at scaled temperatures $T/T_c = 0.50, 0.25, 0.10$. Comparing figure 1 and figure 2, we notice that κ arising from non-equilibrium heating nonlinearity is significantly greater. As figure 2 shows, when we vary the frequency of the power sweeps, the κ arising from non-equilibrium heating nonlinearity increases in magnitude until it reaches a maximum. In comparison, κ arising from the equilibrium supercurrent nonlinearity remains close to zero regardless of frequency, provided that the sweep frequency is far from the pair-breaking frequency.

C. Response time model of nonlinear inductance

The model of nonlinearity described by equation (1) implicitly assumes that the rate at which the equivalent circuit element respond is instantaneous. Our response

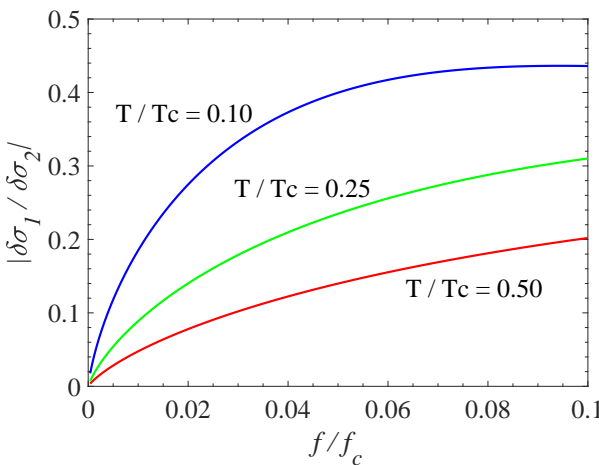


FIG. 2. Dissipative-reactive ratio $\kappa = \delta\sigma_1/\delta\sigma_2$ arising from non-equilibrium heating nonlinearity plotted against scaled frequency f/f_c . Red lines shows the behaviour at scaled tempearture $T/T_c = 0.50$; green lines shows the behaviour at $T/T_c = 0.25$; blue lines shows the behaviour at $T/T_c = 0.10$.

time model instead characterises the nonlinear mechanism by a finite response time τ . The value of τ depends on the dominant physical mechanism responsible for the nonlinearity. For example, the non-equilibrium heating nonlinearity can be characterised by the quasiparticle recombination lifetime [3, 19] which can be controlled by trapping and diffusion [34–36]; likewise, the equilibrium supercurrent nonlinearity can be characterised by a relaxation time [37–40]. In the response time model, the inductance per unit length now takes a modified form:

$$L = L_0 + L_{\text{NL}}, \quad (14)$$

$$L_{\text{NL}}(t) = \frac{L_0}{I_*^2} \int_{-\infty}^t \frac{1}{\tau} \exp\left(-\frac{t-t'}{\tau}\right) I^2(t') dt', \quad (15)$$

where L is the total inductance, L_0 is the unperturbed inductance in the absence of nonlinearity, L_{NL} is the nonlinear contribution to inductance, and t is time. The mathematical form of equation (15) is motivated by the fact that the nonlinear inductance is a kinetic energy phenomenon and is related to even orders of the current. The response time model gives the simplest time dependence to the energy in the system that captures an exponential decay characterised by a timescale τ . In the case of instantaneous response, i.e. $\tau \rightarrow 0$, equations (14) and (15) give

$$L(t) \rightarrow L_0 \left[1 + \left(\frac{I(t)}{I_*} \right)^2 \right] = L_0 + L_{\text{NL},0}(t). \quad (16)$$

Thus in the limit where the nonlinear mechanism is instantaneous, we recover the familiar form of inductance nonlinearity. Here $L_{\text{NL},0}(t)$ is the instantaneous nonlinear inductance.

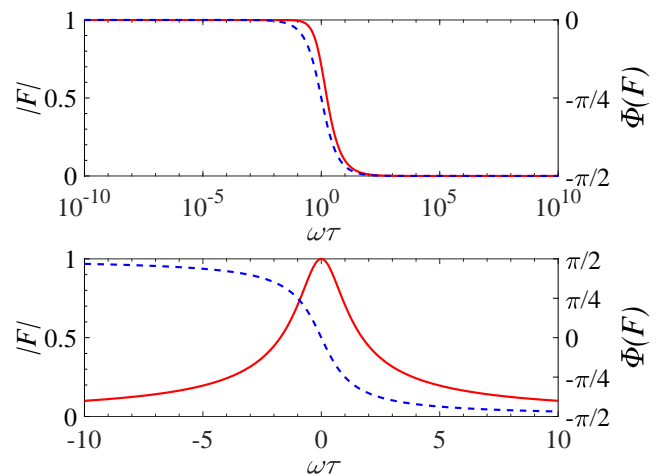


FIG. 3. Top figure: solid red line: magnitude of response time filter $|F|$ plotted against angular frequency scaled by the response time $\omega\tau$; dashed blue line: phase of response time filter $\Phi(F)$ plotted against frequency scaled by the response time $\omega\tau$. The horizontal axis is *logarithmic*. Bottom figure: solid red line: magnitude of response time filter $|F|$ plotted against angular frequency scaled by the response time $\omega\tau$; dashed blue line: phase of response time filter $\Phi(F)$ plotted against frequency scaled by the response time $\omega\tau$. The horizontal axis is *linear*.

It is convenient to work in frequency domain. Applying Fourier transform to the time-dependent inductances, we obtain

$$L_{\text{NL}}(\omega) = \int_{-\infty}^{\infty} L_{\text{NL}}(t) \exp(-i\omega t) dt, \quad (17)$$

$$L_{\text{NL},0}(\omega) = \int_{-\infty}^{\infty} L_{\text{NL},0}(t) \exp(-i\omega t) dt, \quad (18)$$

where ω is the angular frequency. Substituting equation (15) into equation (17), it can be shown that

$$L_{\text{NL}}(\omega) = F(\omega) L_{\text{NL},0}(\omega), \quad (19)$$

$$F(\omega) = \frac{1}{1 + i\omega\tau}, \quad (20)$$

where $F(\omega)$ can be interpreted as a frequency filter applied to the nonlinear inductance as a result of the response time of the underlying microscopic processes. It is important to note that the filter is applied to the perturbations in inductance and not directly to the current or voltage: it places limitations on the *bandwidth* of wave-mixing instead of the maximum frequency of *transmission*.

Figure 3 shows the amplitude and phase of F as a function of normalised frequency $\omega\tau$. In the top panel the frequency axis is *logarithmic*, whereas in the bottom panel it is *linear* and extends over positive and negative frequencies. As expected, F shows low-pass behaviour with the transmission magnitude decreasing rapidly for $\omega\tau > 1$. This will result in a limitation on the amplification bandwidth. As seen in bottom panel, the imaginary

part of the filter dominates at higher frequencies and results in a π phase shift when crossing from $\omega \ll -1/\tau$ to $\omega \gg 1/\tau$. This phase shift will result in a characteristic feature in the gain profile as the next subsection shall describe.

The filter $F(\omega)$ can be straightforwardly applied to coupled mode numerical analyses of wave-mixing in TW-PAs, such as the models presented in [41], chapter 5 of [6], and the appendix of [1]. Coupled mode solvers naturally handle quantities decomposed into their frequency components. The response time frequency filter can thus be applied multiplicatively to the frequency components of the inductances directly. Here we illustrate the process of applying the response time model to the couple mode analysis of a four-wave-mixing TWPA.

In general, current on a transmission line I can be decomposed into its propagation modes I_n such that

$$I = \sum_n I_n, \quad (21)$$

$$I_n = \frac{1}{2} A_n(z) \exp(i\omega_n t - \gamma_n z), \quad (22)$$

$$I_{-n} = I_n^*, \quad (23)$$

where suffix n labels each propagation mode, ω_n is the angular frequency, γ_n is the complex propagation constant in the absence of inductive nonlinearity, and $A_n(z)$ is the position varying amplitude of the current mode. Here the exponential term contains the propagation behaviour of a linear transmission line, and the $A_n(z)$ term contains the effect of the nonlinearity. Equation (15) can be expressed in terms of these propagation modes as follows

$$L_{\text{NL}}(t) = \sum_{i,j} L_{\text{NL}}(I_i, I_j, t) \quad (24)$$

$$L_{\text{NL}}(I_i, I_j, t) = \frac{L_0}{I_*^2} \int_{-\infty}^t \frac{1}{\tau} \exp\left(-\frac{t-t'}{\tau}\right) I_i(t') I_j(t') dt', \quad (25)$$

The transmission line model of a TWPA can be analysed using the telegrapher's equations to give

$$\frac{\partial^2 I}{\partial z^2} = \frac{\partial}{\partial t} \left[LC \frac{\partial I}{\partial t} \right] \quad (26)$$

$$= L_0 C \frac{\partial^2 I}{\partial t^2} + \frac{\partial}{\partial t} \left[L_{\text{NL}} C \frac{\partial I}{\partial t} \right]. \quad (27)$$

We shall refer to the first term as the linear propagation term, and the second term as the nonlinear mixing term. The above equation can be expressed in term of propagation modes, giving

$$\frac{\partial^2 I_n}{\partial z^2} = L_0 C \frac{\partial^2 I_n}{\partial t^2} + \sum_{\omega_i + \omega_j + \omega_k = \omega_n} \frac{\partial}{\partial t} \left[L_{\text{NL}}(I_i, I_j, t) C \frac{\partial I_k}{\partial t} \right]. \quad (28)$$

The response time frequency filter can be applied by noting

$$L_{\text{NL}}(I_i, I_j, t) = F(\omega_i + \omega_j) L_{\text{NL},0}(I_i, I_j, t). \quad (29)$$

In summary, the coupled differential equations governing the evolution of propagation modes are modified by applying the response time frequency filter multiplicatively to the nonlinear mixing term. At this stage, the system of equations can be simplified and solved using the usual routine [6]: cancelling the linear propagation term, applying the slowly-varying-envelope-approximation, and numerically solving the simplified differential equations. In this study, we calculate the gain profiles by applying the response time model to the coupled mode solver described in chapter 5 of [6], which restricts the analysis to pump, signal, and idler modes.

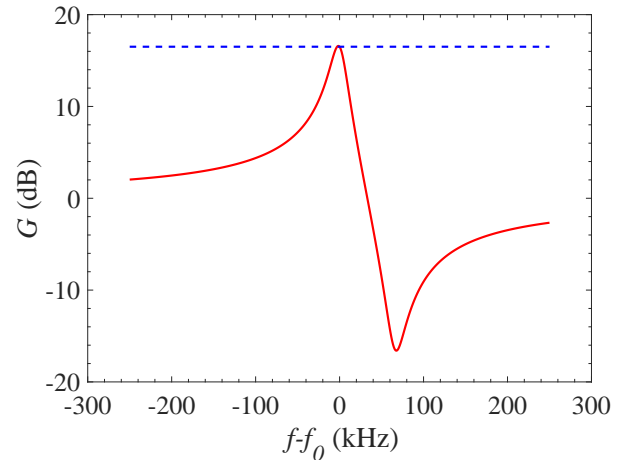


FIG. 4. Power gain G of a Ti TPWA plotted against $f - f_0$ which is the difference between measurement frequency f and pump frequency $f_0 = 10$ GHz. The TWPA has length $l = 0.5$ m and is operated with a pump current of amplitude $I_{p,0} = 0.15 I_*$, where I_* is the characteristic nonlinear scale of current. Solid red line: the underlying nonlinearity has response time of $\tau = 1/(2\pi \times 10^4)$ s; dashed blue line: the underlying nonlinear response is instantaneous.

Figure 4 shows the simulated gain profile of a 0.5 m long Ti TWPA. The solid red line assumes $\tau = 1/(2\pi \times 10^4)$ s whereas the dash blue line assumes that the underlying nonlinear response is instantaneous. As seen in the figure, the response time filter restricts the bandwidth of the gain profile. This bandwidth restriction effect can be illustrated by considering the frequency mixing modes that contribute to signal amplification. In a 4-wave-mixing system, *one of* the mixing modes is as follows: an idler at ω_i and a pump at ω_p generates their difference frequency $\Delta\omega = \omega_p - \omega_i = \omega_s - \omega_p$ in the inductance. This difference frequency simultaneously mixes with ω_p to generate amplified signal $\omega_p + \Delta\omega = \omega_s$. In total, two pump modes are coupled with one idler mode to generate one signal mode: this mixing mode is thus allowed by 4-wave-mixing. The slow response time filtering however,

attenuates the amplitude of L_{NL} where $\Delta\omega > 1/\tau$. This leads to smaller gain at larger $\Delta\omega$. In the gain profile this effect restricts the bandwidth to the order of $1/\tau$. The other mixing modes can be shown to be similarly affected by the inductance response time filtering.

Another characteristic feature demonstrated by figure 4 is the gain dip at $f - f_0 \sim 60$ kHz. This effect can be attributed to the π phase flipping of $F(\omega)$ when the angular frequency crosses from $\omega \ll -1/\tau$ to $\omega \gg 1/\tau$. The output signal consist of the original signal $I_{s,0}$ and the signal generated by nonlinear inductance $I_{s,\text{NL}}$. As the two contributions are added together, the phase flipping at signal frequencies higher than the pump frequency induces a destructive interference effect. This interference effect is hidden when $I_{s,\text{NL}} \ll I_{s,0}$ or $I_{s,\text{NL}} \gg I_{s,0}$. It is obvious on the gain profile when $I_{s,\text{NL}} \sim I_{s,0}$. If, in simulations, a new filter is imposed such that $F_{\text{new}}(\omega) = |F(\omega)|$, the dip in gain disappears. This confirms that the origin of the dip stems from the phase of the response time filtering.

III. MEASUREMENTS OF AL AND TI TRAVELLING-WAVE DEVICES

The results in this section were obtained from measurements of superconducting Al and Ti TWPA devices at temperature of 0.1 K. Al and Ti were chosen because calculations based on the BCS theory have shown that these materials have low onset power with respect to the equilibrium supercurrent nonlinearity [5, 6]. The devices presented in this work were based on co-planar waveguide (CPW) geometries. The devices were designed to have close to 50Ω characteristic impedance and high kinetic inductance ratios. Films were deposited onto 2-inch SEMI standard Si wafers by DC magnetron sputtering at a base pressure of 2×10^{-10} Torr or below. The samples were attached to the cold stage of an adiabatic demagnetization refrigerator and the temperature was monitored using a calibrated ruthenium oxide thermometer. The measurements of power transmission and phase shift were obtained using a vector network analyser (VNA). In this study, the power transmission T_{out} is defined as the ratio between the power received at the VNA P_{in} and the power delivered by the output of the VNA P_{out} . It includes both the effect of the TWPA under test as well as the attenuation due to coaxial cables in the cryostat, which was about 55 dB at 8.0 GHz. When all quantities are measured in units of dB, T_{out} is given by $T_{\text{out}} = P_{\text{in}} - P_{\text{out}}$.

A. Dissipative-reactive ratios

The dissipative-reactive ratio of a device can be inferred from measurements of its nonlinear power attenuation and nonlinear phase shift in response to increasing readout power. Nonlinear power attenuation T_{α} is

a function of the input power P_{in} , and is defined as $T_{\alpha}(P_{\text{in}}) = T_{\text{out},0} - T_{\text{out}}(P_{\text{in}})$, where $T_{\text{out},0}$ is the power transmission ratio at very low input power below the onset of nonlinearity. The phase shift $\Delta\Phi$ gives the phase difference between the output signal and the input signal. The nonlinear phase shift $\Delta\Phi_{\text{NL}}$ is given by $\Delta\Phi_{\text{NL}}(P_{\text{in}}) = \Delta\Phi_0 - \Delta\Phi(P_{\text{in}})$, where $\Delta\Phi_0$ is the phase shift at very low input power below the onset of nonlinearity.

From transmission line theory, for small perturbations, it can be shown that [6, 42]

$$T_{\alpha} = 8.69 L \delta\alpha \text{ dB}, \quad (30)$$

$$\Delta\Phi_{\text{NL}} = |L \delta\beta|, \quad (31)$$

where L is the length of the transmission line, $\delta\alpha$ is the change in attenuation constant, $\delta\beta$ is the change in phase constant. $\delta\alpha$ and $\delta\beta$ are related to the change in full propagation constant $\delta\gamma$ by $\delta\alpha + i\delta\beta = \delta\gamma$. Further, at small input power, it can be shown that

$$\delta\gamma = C_{\text{geom}} \delta\sigma \quad (32)$$

$$\kappa = \frac{\delta\sigma_1}{\delta\sigma_2} = \frac{\delta\alpha}{\delta\beta}, \quad (33)$$

where C_{geom} is a constant of proportionality arising from device geometry. Thus κ for a particular device can be deduced by relating its nonlinear attenuation T_{α} to its nonlinear phase shift $\Delta\Phi_{\text{NL}}$.

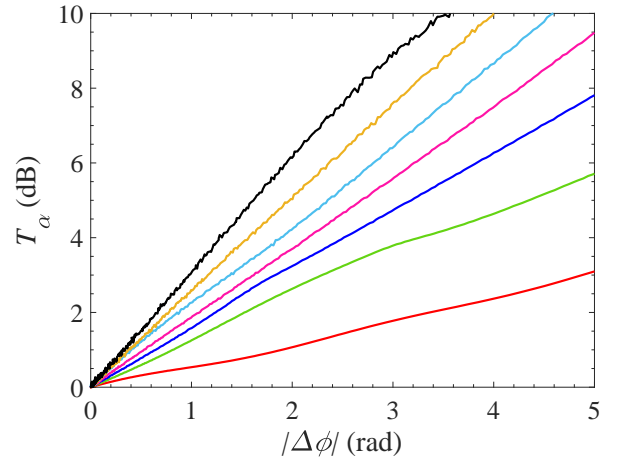


FIG. 5. Nonlinear power loss P_{α} against the magnitude of nonlinear phase shift $|\Delta\Phi|$ for a TWPA based on 50 cm long, 75 nm thick Ti CPW transmission line. Frequencies of the underlying power sweep are 1.0 GHz, 2.0 GHz, 3.0 GHz, 4.0 GHz, 5.0 GHz, 6.0 GHz, and 7.0 GHz, corresponding to plots of increasing steepness in their gradients.

Figure 5 shows the nonlinear power loss P_{α} against the magnitude of nonlinear phase shift $|\Delta\Phi|$ for a Ti CPW device at frequencies 1.0 GHz, 2.0 GHz, 3.0 GHz, 4.0 GHz, 5.0 GHz, 6.0 GHz,

and 7.0 GHz. As seen in the plot, as frequency increases, so does the relative magnitude of the dissipative nonlinearity.

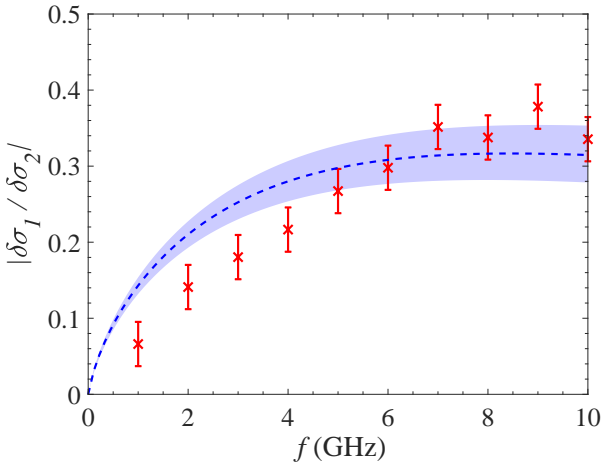


FIG. 6. Dissipative-reactive ratio $\kappa = \delta\sigma_1/\delta\sigma_2$ plotted against frequency f . The red points show data for a Ti CPW transmission line, as obtained by fitting the gradients of the lines in figure 5; the blue dashed line shows the best fit using the non-equilibrium heating model. Transition temperature T_c is the fit variable and experimentally recorded bath temperature $T = 0.15$ K is a fixed input to the model. The best fit transition temperature is 0.44 K with a 90% confidence interval of 0.30 K to 0.66 K. The range of behaviour described by the 90% confidence interval is shown by the light blue region surrounding the best fit line.

Figure 6 shows the experimentally measured κ against frequency f . The red points show data for the Ti CPW device described previously, as obtained by fitting the gradients of the lines in figure 5. The blue dashed line shows the least squares fit using the non-equilibrium heating model. The bath temperature was fixed at the experimentally measured value $T = 0.15$ K, leaving the transition temperature T_c as the only fitting variable. We have assumed that Ti is a BCS superconductor and can be described by $\Delta_0 = 1.764 k_B T_c$. The best fit transition temperature is 0.44 K with a 90% confidence interval of 0.30 K to 0.66 K. The range of behaviour described by the 90% confidence interval is shown by the light blue region surrounding the best fit line. As seen in the figure, the magnitude and frequency trend of κ is similar to that predicted by non-equilibrium heating. Small deviations to the model may be the result of 1) on-chip heating due to measurements performed at high powers [6], 2) a small contribution from the equilibrium supercurrent nonlinearity increasing the measured reactive nonlinearity, and 3) spurious ground plane resonance features due to the large size of the chip [43]. The variations occurring at the range of 6 GHz to 10 GHz is used as an estimate on the magnitude of uncertainties and secondary effects, as shown in the error bars of figure 6. The best fit transition temperature of 0.44 K is consistent with di-

rect measurements of the transition temperatures of Ti in the literature, which span the range of 0.37 K to 0.59 K [44, 45]. Overall, the behaviour of the Ti transmission line is well described by the model, suggesting that the non-equilibrium heating mechanism contributes strongly to the nonlinearity displayed by the Ti device.

B. Gain profiles

In this study, the power gain G of a device is defined as the ratio between the output signal power transmission in the presence of a strong pump current $T_{\text{out},P}$ generated by a signal generator and the output signal power transmission in the absence of a strong pump current $T_{\text{out},0}$. Since both $T_{\text{out},P}$ and $T_{\text{out},0}$ are measured in units of dB, the power gain is given by $G = T_{\text{out},P} - T_{\text{out},0}$.

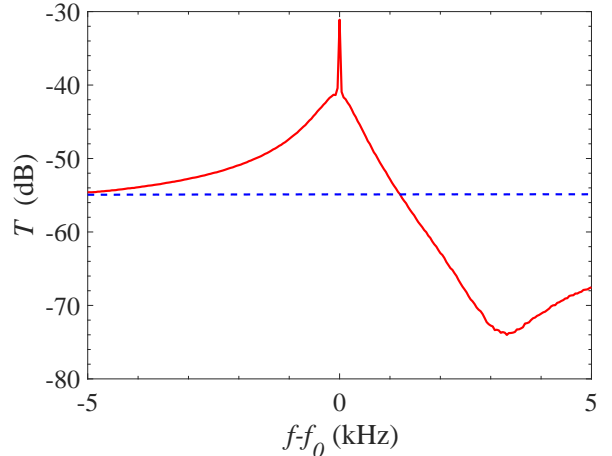


FIG. 7. Power transmission measurement of an Al CPW TWPA. The horizontal axis indicates the difference between measurement frequency f and pump frequency $f_0 = 8.0$ GHz. Pump power from at the output of signal generator is 14.66 dBm. Solid red line: power transmission in the presence of pump current; dashed blue line: power transmission in the absence of pump current. The blue line characterises the losses in the test system. The difference between the red and blue line indicates device gain.

Figure 7 shows the power transmission measurement of a CPW TWPA based on Al. The TWPA transmission line is biased at pump frequency $f_0 = 8.0$ GHz with a pump power of 14.66 dBm, as measured at the output of the VNA. The solid red line shows power transmission in the presence of pump current whereas the dashed blue line shows power transmission in the absence of pump current. The transmission spike at $f - f_0 = 0$ kHz is the unsuppressed pump current. As seen in the figure, without the biasing pump current, the transmission of the TWPA line is at -55 dB. This attenuation is mainly a result of losses from long coaxial cables which are external to the chip. Once the pump has been switched on, the signal is amplified to as high as -41 dB. Thus a maxi-

mum on-chip gain of 14 dB is obtained. Interestingly, the 3 dB bandwidth of the device is only around 1 kHz, instead of in the range of GHz. The observation of this limited bandwidth strongly motivated the formulation of the response time model of nonlinear inductance.

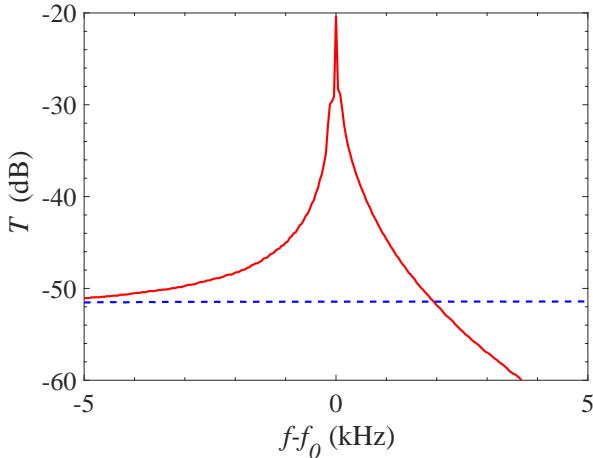


FIG. 8. Power transmission measurement of an Al CPW TWPA, optimised for gain. The horizontal axis indicates the difference between measurement frequency f and pump frequency $f_0 = 7.0$ GHz. Pump power from at the output of signal generator is 13.80 dBm. Solid red line: power transmission in the presence of pump current; dashed blue line: power transmission in the absence of pump current. The blue line characterises the losses in the test system. The difference between the red and the blue line indicates device gain.

Figure 8 shows the power transmission measurement of the same device with an optimised pump power of 13.80 dBm at $f_0 = 7.0$ GHz. Optimisation is necessary because the TWPA materials display strong dissipative nonlinearity at high powers. It is important to operate the device so that the gain is not depressed heavily by the sharply increasing dissipation. This optimisation is performed by slowly varying the magnitude of the pump power at each frequency to obtain the largest gain. As figure 8 demonstrates, by optimising the pump current, we are able to obtain peak gain of more than 20 dB.

Figure 9 shows a comparison between the gain obtained experimentally and the gain calculated using the response time nonlinearity model. We have included 3 dB of best fit dissipative loss in this calculation to account for the fact that the presence of a strong pump also introduces nonlinear dissipation, as discussed in earlier sections. The best fit τ of 3.27×10^{-4} s is used. As seen in the figure, the model describes experimental data very well and captures the following key characteristic behaviour: 1) height of gain around pump frequency; 2) 3 dB bandwidth; 3) the gain dip at ~ 3.2 kHz; and 4) the gradients of the rise and fall in gain around the maximum. The measured timescale of 3.27×10^{-4} s is much shorter than the timescale of the equilibrium superconductor nonlinearity, which should be in the range of nanoseconds to pi-

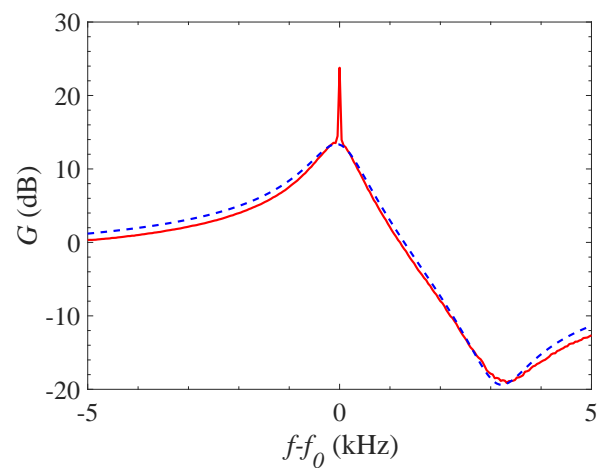


FIG. 9. Gain data of an Al CPW TWPA. The horizontal axis indicates the difference between measurement frequency f and pump frequency $f_0 = 8.0$ GHz. Pump power from at the output of signal generator is 14.66 dBm. Solid red line: gain data obtained experimentally; dashed blue line: gain data as calculated using response time nonlinearity model. The best fit τ of 3.27×10^{-4} s is used.

coseconds [37–40], but is similar to the timescale of quasi-particle recombination, which should be in the range of milliseconds to microseconds [3, 46, 47]. This suggests that the non-equilibrium heating mechanism contributes strongly to the nonlinearity displayed by the Al device.

IV. CONCLUSIONS

In this study, we have described a method of characterising the underlying nonlinearity of a superconducting material by its dissipative-reactive ratio and the response time of its nonlinear mechanism. Both quantities are important in determining the performance of TWPs, such as in terms of added noise, maximum gain, and bandwidth. We discussed how different nonlinearities, for example the equilibrium supercurrent nonlinearity and the non-equilibrium heating nonlinearity, can manifest themselves very differently in terms of their dissipative-reactive ratios and response times. A nonlinearity with low dissipation and fast response time such as the equilibrium supercurrent nonlinearity can be distinguished easily from a nonlinearity with high dissipation and slow response time such as the non-equilibrium heating nonlinearity.

Experimentally, the dissipative-reactive ratio can be deduced from measurements of attenuation and phase shift as functions of input power level; whereas the response time of the underlying nonlinearity can be extracted from measurements of gain as a function of signal frequency. We have fabricated TWPs based on Al and Ti, and characterised their nonlinearities using our analysis. Our results suggest that for both Al and Ti,

the dominant underlying nonlinear mechanism differ significantly from the equilibrium supercurrent nonlinearity. Instead, the measured dissipative-reactive ratios and response times are quantitatively similar to predictions for the non-equilibrium heating nonlinearity.

Currently in the literature, all TWPs that have successfully reported broad-band amplification are based on alloy or amorphous superconductors such as NbTiN, NbN, TiN, and WSi [1, 43, 48]. Important research should be performed to investigate the significance of non-equilibrium nonlinear mechanisms in these materials. Interestingly, these materials have also been shown to have quasiparticle lifetimes that are several orders of magnitude smaller compared to that of elemental superconductors [46, 49–51]. In the context of this study, two explanations can be offered regarding their success at achieving broad-band amplification: 1) For some materials, the nonlinear behaviour is still dominated by the non-equilibrium heating mechanism. However, the short quasiparticle lifetimes allow the bandwidths of the amplification processes to be in the GHz range. 2) The onset power of the non-equilibrium heating mechanism increases as the lifetime decreases [18, 19]. When the equilibrium supercurrent nonlinearity has the smaller onset

power, the amplifier can be operated at power levels that achieve amplification mainly through the equilibrium supercurrent nonlinearity. Under this operating condition, the fast response time of the equilibrium supercurrent nonlinearity allows the device to achieve broad-band amplification. Theoretical research should be done to quantitatively compare the onset powers of different nonlinear mechanisms using commonly measured material properties, such as critical current density and quasiparticle recombination time. It is valuable to explore design schemes that suppress non-equilibrium nonlinear mechanisms in order to reduce their limitations on the performance of TWPs.

Beyond the immediate context of TWPs, our method of characterising nonlinearities can prove useful in the analysis of other superconducting nonlinear devices. Examples of these devices include parametric up-converters [4], kinetic inductance spectrometers [52], fibre based nonlinear devices [53], and resonator parametric amplifiers [54]. Similar to a TWP, these nonlinear devices also exploit the underlying superconducting nonlinearities. Dissipative effects and rate-limiting response times are thus likewise important to their operation and performance. A detailed analysis of these effects in the context of resonator parametric amplifiers can be found in [8].

* sz311@cam.ac.uk

- ¹ B. H. Eom, P. K. Day, H. G. LeDuc, and J. Zmuidzinas, *Nat. Phys.* **8**, 623 (2012).
- ² M. Malnou *et al.*, *PRX Quantum* **2**, 010302 (2021).
- ³ J. Zmuidzinas, *Annu. Rev. Condens. Matter Phys.* **3**, 169 (2012).
- ⁴ A. S. Kher, *Superconducting Nonlinear Kinetic Inductance Devices*, PhD thesis, California Institute of Technology, 2017.
- ⁵ S. Zhao, S. Withington, D. J. Goldie, and C. N. Thomas, *Journal of Low Temperature Physics* **199**, 34 (2020).
- ⁶ S. Zhao, *Physics of Superconducting Travelling-Wave Parametric Amplifiers*, PhD thesis, University of Cambridge, 2021.
- ⁷ S. Zhao and S. Withington, *Journal of Physics D: Applied Physics* **54**, 365303 (2021).
- ⁸ C. N. Thomas, S. Withington, and S. Zhao, Effects of reactive, dissipative, and rate-limited nonlinearity on the behaviour of superconducting parametric amplifiers, 2022.
- ⁹ M. Tinkham, *Introduction to Superconductivity*, 2nd ed. (McGraw-Hill, New York, 1994).
- ¹⁰ R. Parmenter, RCA (Radio Corporation of America) Review (US) **23** (1962).
- ¹¹ D. J. Goldie and S. Withington, *Superconductor Science and Technology* **26**, 015004 (2012).
- ¹² P. J. de Visser *et al.*, *Applied Physics Letters* **100**, 162601 (2012), <https://doi.org/10.1063/1.4704151>.
- ¹³ P. J. de Visser *et al.*, *Phys. Rev. Lett.* **112**, 047004 (2014).
- ¹⁴ A. Anthore, H. Pothier, and D. Esteve, *Physical review letters* **90**, 127001 (2003).
- ¹⁵ S. Zhao, S. Withington, D. J. Goldie, and C. N. Thomas, *Journal of Physics D: Applied Physics* **53**, 345301 (2020).
- ¹⁶ P. J. de Visser, S. Withington, and D. J. Goldie, *Journal of Applied Physics* **108**, 114504 (2010), <https://doi.org/10.1063/1.3517152>.
- ¹⁷ T. Guruswamy, *Nonequilibrium behaviour and quasiparticle heating in thin film superconducting microwave resonators*, PhD thesis, University of Cambridge, 2018, <https://doi.org/10.17863/CAM.24510>.
- ¹⁸ A. Rothwarf and B. N. Taylor, *Phys. Rev. Lett.* **19**, 27 (1967).
- ¹⁹ C. N. Thomas, S. Withington, Z. Sun, T. Skyrme, and D. J. Goldie, *New Journal of Physics* **22**, 073028 (2020).
- ²⁰ A. V. Semenov, I. A. Devyatov, P. J. de Visser, and T. M. Klapwijk, *Phys. Rev. Lett.* **117**, 047002 (2016).
- ²¹ W. Belzig, F. K. Wilhelm, C. Bruder, G. Schön, and A. D. Zaikin, *Superlattices and Microstructures* **25**, 1251 (1999).
- ²² A. I. Larkin and Y. N. Ovchinnikov, *Journal of Experimental and Theoretical Physics* **92**, 519 (2001).
- ²³ J. McDonald, *Nonlinear response of superconductors to alternating fields and currents*, PhD thesis, Iowa State University, 1997.
- ²⁴ K. K. Likharev, *Rev. Mod. Phys.* **51**, 101 (1979).
- ²⁵ J. Gao *et al.*, *Applied Physics Letters* **92**, 212504 (2008), <https://doi.org/10.1063/1.2937855>.
- ²⁶ R. de L. Kronig, *J. Opt. Soc. Am.* **12**, 547 (1926).
- ²⁷ H. A. Kramers, *Atti Cong. Intern. Fisica (Transactions of Volta Centenary Congress) Como* **2**, 545 (1927).
- ²⁸ K. D. Usadel, *Phys. Rev. Lett.* **25**, 507 (1970).
- ²⁹ G. Brammertz *et al.*, *J. Appl. Phys.* **90**, 355 (2001), <https://doi.org/10.1063/1.1376411>.
- ³⁰ J. M. Martinis, G. Hilton, K. Irwin, and D. Wollman, *Nucl. Instrum. Meth. A* **444**, 23 (2000).
- ³¹ S. B. Nam, *Phys. Rev.* (1967).

³² S. Zhao, D. J. Goldie, S. Withington, and C. N. Thomas, Supercond. Sci. Tech. **31**, 015007 (2018).

³³ M. R. Vissers *et al.*, Applied Physics Letters **107**, 062601 (2015), <https://doi.org/10.1063/1.4927444>.

³⁴ D. J. Goldie, N. E. Booth, C. Patel, and G. L. Salmon, Phys. Rev. Lett. **64**, 954 (1990).

³⁵ M. Loidl *et al.*, Nuclear Instruments and Methods in Physics Research Section A: Accelerators, Spectrometers, Detectors and Associated Equipment **465**, 440 (2001).

³⁶ C. Wang *et al.*, Nature Communications **5**, 5836 (2014).

³⁷ G. Lucas and M. J. Stephen, Phys. Rev. **154**, 349 (1967).

³⁸ B. Mattoo and Y. Singh, Pramana **19**, 483 (1982).

³⁹ M. E. C. Stuivinga, *Voltage-carrying states in superconducting microstrips*, PhD thesis, Delft University of Technology, 1983.

⁴⁰ B. A. Mattoo and Y. Singh, Progress of Theoretical Physics **70**, 51 (1983), <https://academic.oup.com/ptp/article-pdf/70/1/51/5370405/70-1-51.pdf>.

⁴¹ S. Zhao, S. Withington, D. J. Goldie, and C. N. Thomas, Journal of Physics D: Applied Physics **52**, 415301 (2019).

⁴² S. Zhao, S. Withington, D. J. Goldie, and C. N. Thomas, Superconductor Science and Technology (2018).

⁴³ A. A. Adamyan, S. E. de Graaf, S. E. Kubatkin, and A. V. Danilov, Journal of Applied Physics **119**, 083901 (2016), <https://doi.org/10.1063/1.4942362>.

⁴⁴ M. C. Steele and R. A. Hein, Phys. Rev. **92**, 243 (1953).

⁴⁵ S. Zhao, D. J. Goldie, C. N. Thomas, and S. Withington, Superconductor Science and Technology **31**, 105004 (2018).

⁴⁶ R. Barends *et al.*, Phys. Rev. Lett. **100**, 257002 (2008).

⁴⁷ P. J. de Visser *et al.*, Journal of Low Temperature Physics **167**, 335 (2012).

⁴⁸ S. Goldstein *et al.*, Applied Physics Letters **116**, 152602 (2020), <https://doi.org/10.1063/5.0004236>.

⁴⁹ T. Guruswamy, D. J. Goldie, and S. Withington, Superconductor Science and Technology **28**, 054002 (2015).

⁵⁰ R. M. J. Janssen *et al.*, Journal of Low Temperature Physics **167**, 354 (2012).

⁵¹ B. A. Mazin, Superconducting materials for microwave kinetic inductance detectors, 2020, 2004.14576.

⁵² F. B. Faramarzi *et al.*, Journal of Low Temperature Physics **199**, 867 (2020).

⁵³ J. P. Goure, I. Verrier, and J. P. Meunier, Journal of Physics D: Applied Physics **22**, 1791 (1989).

⁵⁴ E. A. Tholén, A. Ergül, K. Stannigel, C. Hutter, and D. B. Haviland, Physica Scripta **2009**, 014019 (2009).